Journal of the Serbian Society for Computational Mechanics / Vol. 19 / No. 2, 2025 / pp 62-79 / original paper
(10.24874/jsscm.2025.19.02.05)

THREE-DIMENSIONAL NUMERICAL INVESTIGATION OF STATIC AERODYNAMIC COEFFICIENTS FOR AN ARTILLERY PROJECTILE USING STEADY-STATE RANS METHODOLOGY

Damir D. Jerković[1*] [000-0001-5182-7057], Abdellah Ferfouri[1] [009-0005-5593-7794], Nebojša Hristov[1] [000-0002-8163-2223], Toufik Allouche[1] [009-0008-8047-667X], Igor Radisavljević[2] [0000-0002-8523-0993] and Mladen Josijević[3] [0000-0001-9619-0897]

[1]University of Defence - Military Academy, Veljka Lukića Kurjaka 33, 11042 Belgrade, Serbia
e-mail: damir.jerkovic@va.mod.gov.rs, fer-abdel@hotmail.com, nebojsahristov@gmail.com, toufik.allouche@gmail.com
[2]Military Technical Institute, Ratka Resanovića 1, 11030 Belgrade, Serbia
e-mail: radisavljevicigorbg@gmail.com
[3]University of Kragujevac, Faculty of Engineering, Sestre Janjić 6, 34000 Kragujevac, Serbia
e-mail: mladenjosijevic@gmail.com
*c*orresponding author*

Abstract

This paper presents a numerical analysis of the static aerodynamic coefficients of the 155 mm M107 spin-stabilized projectile over Mach numbers ranging from 0.5 to 3.0. Building upon previous axisymmetric 2D research, a 3D steady-state RANS approach was implemented using an optimized structured O-grid topology to resolve the asymmetric flow field. The performance of the SST k-ω and Realizable k-ε turbulence models was evaluated at angles of attack of 2°, 5°, and 8° to determine the coefficients of axial force, normal force, and pitching moment. Numerical results were compared with experimental measurements for the M107 and M101 projectiles. The results demonstrate that the selected numerical approach effectively predicts the considered aerodynamic loads, ensuring a reliable extraction of the static aerodynamic derivatives. This work confirms that the computational methodology provides an efficient tool for generating high-fidelity aerodynamic data for trajectory and stability assessments.

Keywords: spin-stabilized projectile, static aerodynamic coefficients, steady-state simulations, O-grid topology, RANS models.

1. Introduction

Precise estimation of aerodynamic loads is a fundamental requirement for describing the free flight and trajectory of spin stabilized projectiles. Among these loads, aerodynamic drag is a primary factor that directly influences range and impact point accuracy. This force results from pressure distribution, skin friction, and complex base region flow (Ferfouri et al. 2025). However, a complete flight stability analysis also requires a precise characterization of other static and dynamic aerodynamic parameters. Specifically, the normal force and its associated pitching moment govern the gyroscopic and dynamic stability of the projectile throughout its flight regime

(Doraiswamy & Candler 2008). In particular, rotationally stabilized bodies may develop a significant yaw angle during launches at high firing elevations. Understanding these aerodynamic characteristics at various angles of attack (AoA) is critical for improving fire control solutions and impact accuracy (DeSpirito 2017).

Modern aerodynamic research typically relies on three main approaches: semi empirical methods, experimental testing, and Computational Fluid Dynamics (CFD) (Roy 2012). While semi empirical codes such as PRODAS provide rapid estimations, their accuracy is often limited outside of recommended data ranges (Ko et al. 2020). Experimental techniques such as wind tunnel testing and aeroballistic ranges are highly valuable but present challenges involving wall interference and high operational costs (Fresconi & Celmins 2018). Consequently, computational analyses employing the Reynolds-Averaged Navier–Stokes (RANS) equations have become an indispensable tool. This computational wind tunnel approach enables designers to obtain the complete aerodynamic dataset required for predicting in-flight behavior while using reasonable computational resources (Silton 2011). RANS turbulence models offer a reliable balance between efficiency and accuracy for estimating static aerodynamic derivatives during the design phase of modern munitions (DeSpirito & Heavey 2004; DeSpirito et al. 2009).

Previous research by the authors focused on two-dimensional (2D) axisymmetric simulations aimed at assessing the influence of different grid configurations and RANS turbulence approaches on drag prediction (Ferfouri et al. 2025). This earlier study showed that using an O-shaped grid arrangement in combination with the Realizable k-ε turbulence model yields superior accuracy in predicting drag at zero yaw. However, axisymmetric 2D simulations cannot resolve the circumferential flow variations that develop at non-zero angles of attack and therefore do not capture the asymmetric pressure, shock, and wake features responsible for the normal force and the pitching moment. These fundamental limitations restrict the applicability of 2D approaches to drag prediction only and exclude the extraction of static aerodynamic derivatives required for trajectory and stability analyses. To address this limitation, a three-dimensional (3D) steady-state formulation is required to resolve these asymmetric flow structures and to enable direct computation of the normal force and pitching moment together with their static derivatives (Chughtai et al. 2019). Previous investigations have confirmed that steady-state RANS simulations provide strong agreement with experimental measurements for static aerodynamic coefficients at moderate angles of attack, typically below 20 degrees (DeSpirito 2008; Ko et al. 2020). Furthermore, static aerodynamic coefficients remain well predicted even when the projectile geometry is modeled without the engraving caused by rifling (Silton 2005).

The current study builds upon these findings to assess the performance of the SST k-ω and Realizable k-ε turbulence models within a 3D steady-state methodology. This study highlights the key contribution of applying fully 3D steady-state RANS together with an optimized O-topology structured hexahedral mesh validated by grid-independence studies and strict near-wall resolution. A procedure for extracting static aerodynamic derivatives from the 3D simulations is presented and cross-checked against aeroballistic measurements, and practical solver and modeling choices are reported to demonstrate that high-fidelity 3D aerodynamic data can be obtained efficiently for large-caliber ammunitions. This approach is particularly important for capturing the complex flow interactions and non-linearities observed in the transonic regime (Ko et al. 2020). While the normal force and its pitching moment often exhibit linear behavior at low AoA values, the axial force shows quadratic dependence (Fresconi & Celmins 2018). The numerical results are compared with experimental measurements for the M107 and M101 projectiles to confirm that the selected numerical settings are appropriate for generating reliable aerodynamic data for trajectory and stability assessments.

This article is organized across five sections. Following this introduction, the second part describes the computational approach. The third section details the approach for determining

aerodynamic coefficient derivatives. The fourth section presents the results and discussions, including the validation against experimental data. Finally, the main conclusion is summarized in the fifth section.

2. Computational approach

The aerodynamic environment surrounding a spin-stabilized projectile is defined by complex air-surface interactions occurring within high-Reynolds number regimes. These flow patterns are primarily dictated by the projectile external configuration, flight velocity, and the specific state of the surrounding atmosphere. Consequently, high-fidelity CFD simulations necessitate sophisticated modeling strategies to effectively resolve near-wall shear layers and wake regions.

2.1 Governing equations

To resolve the compressible flow field, the governing conservation laws, including both the RANS-based continuity and momentum equations, are defined as follows (Ansys Inc. 2013; Ferfouri et al. 2023):

$$\frac{\partial \rho}{\partial t}+\frac{\partial(\rho u_i)}{\partial x_i}=0 \tag{1}$$

$$\frac{\partial(\rho u_i)}{\partial t}+\frac{\partial(\rho u_i u_j)}{\partial x_j}=-\frac{\partial P}{\partial x_i}+\frac{\partial}{\partial x_j}\left[\mu\left(\frac{\partial u_i}{\partial x_j}+\frac{\partial u_j}{\partial x_i}-\frac{2}{3}\delta_{ij}\frac{\partial u_l}{\partial x_l}\right)\right]+\frac{\partial}{\partial x_j}\left(-\rho\overline{u_i' u_j'}\right) \tag{2}$$

These equations are coupled with the ideal gas law, assuming ideal gas behavior for the air surrounding the projectile body:

$$P=\rho RT \tag{3}$$

In order to close the RANS equations, the Boussinesq approximation (Ansys Inc. 2013) is adopted to represent the Reynolds stress tensor. This method effectively correlates the turbulent stresses with the gradients of the mean velocity through the following expression:

$$-\rho\overline{u_i' u_j'}=\mu_t\left(\frac{\partial u_i}{\partial x_j}+\frac{\partial u_j}{\partial x_i}\right)-\frac{2}{3}\left(\rho k+\mu_t\frac{\partial u_k}{\partial x_k}\right)\delta_{ij} \tag{4}$$

Where t is the time, x is the geometric coordinate, u is the mean velocity, ρ is the air density, u' is the fluctuating velocity, μ is the molecular viscosity, P is the mean pressure, δ_{ij} is the Kronecker delta, k is turbulent kinetic energy, μ_t is the turbulent viscosity, R specific gas constant, and T is the temperature.

Following the validation and performance analysis conducted in our previous study (Ferfouri et al. 2025), the two turbulence models, Realizable k-ε and SST k-ω, are employed for this 3D investigation. These two-equation RANS closures are selected for their proven trade-off between computational cost and predictive reliability in projectile aerodynamics. Both models introduce a pair of supplementary transport equations governing the turbulent kinetic energy k and its respective dissipation rates ε or ω to account for the convective and diffusive transport of turbulent quantities in the flow. The detailed mathematical formulations of these RANS models are not reproduced here, as they are thoroughly documented in our previous study (Ferfouri et al. 2025) and are well-established within the existing literature (Menter 1994; Shih et al. 1995; Ansys Inc. 2013).

2.2 Hypotheses and boundary conditions

The current 3D research maintains the same fundamental hypotheses as the previous study (Ferfouri et al. 2025), adopting a steady-state RANS approach to evaluate static aerodynamic coefficients. This method is justified by the fact that the transit time of fluid elements within the domain is significantly shorter than the characteristic time scales of boundary condition variations. While our previous work (Ferfouri et al. 2025) confirmed the reliability of the steady-state assumption for drag prediction at zero-yaw, it is well-established in the literature that steady-state RANS simulations also provide strong consistency with experimental measurements for the remaining static aerodynamic coefficients, specifically those of the normal force C_N and pitching moment C_m (DeSpirito & Heavey 2004; Silton 2005; DeSpirito et al. 2009; DeSpirito 2017; Ko et al. 2020). The atmospheric environment is modeled according to ICAO standards (ICAO 1993), treating air as a compressible ideal gas with viscosity determined by the three-coefficient Sutherland law. In this 3D study, the free-stream Reynolds number varies between 1.2×10^6 and 2.4×10^6 based on the projectile caliber. The boundary conditions are defined to match physical flight conditions: an adiabatic no-slip wall treatment is imposed on the projectile surface, while a pressure far-field condition is used for domain initialization and to represent the undisturbed flow. Isentropic relations for an ideal gas are employed to calculate the far-field data, using standard sea-level reference conditions (p_0 = 101,325Pa and T_0 = 288.15K) as the reference. Furthermore, the turbulence intensity and viscosity ratio prescribed at the inflow are kept, respectively, at 2% and 10.

2.3 Projectile geometry

The study focuses on the 155 mm M107 artillery projectile, as shown in Fig. 1. While the earlier 2D study (Ferfouri et al. 2025) was limited to drag prediction at zero-yaw, this 3D model allows for the determination of the coefficients (C_N and C_m) of normal force and pitching moment in addition to the axial force coefficient C_X. To guarantee an accurate representation of the physical configuration, the geometric dimensions follow the data reported in (McCoy 1998). The projectile model is characterized by a total length of 4.52 cal., with the center of gravity (CG) located 2.96 cal. measured from the nose. Maintaining these exact proportions is essential for accurately capturing the flow behavior across the subsonic, transonic, and supersonic regimes.

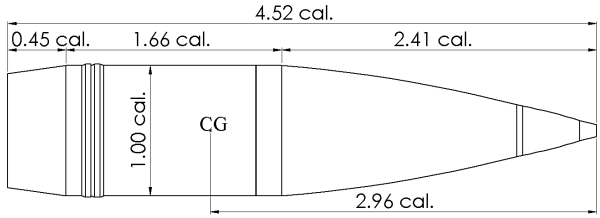

Fig. 1. Projectile dimensions in calibers.

2.4 Grid generation

Based on the superior performance of the O-topology identified in our previous 2D research (Ferfouri et al. 2025), a 3D structured hexahedral mesh was constructed. The grid generation was performed using Gambit software, utilizing a multi-block strategy to ensure high quality and avoid cell deformation. The 3D computational domain (Fig. 2) was built by rotating the optimized 2D O-grid layout around the projectile longitudinal axis, resulting in a structured configuration composed of eight identical 45-degree segments, each containing five blocks. The specific characteristics of this 3D computational domain are presented in Table 1.

To ensure accurate boundary layer capturing, the first cell spacing is kept at 5×10^{-6} cal. (7.6×10^{-4} mm), maintaining a y^+ value below 0.5. The number of nodes on the projectile surface remains the same as the validated 2D setup (Ferfouri et al. 2025), and for these steady-state RANS simulations, 80 cells are distributed uniformly in the circumferential direction. Furthermore, the grid stretching ratios toward the far-field were kept identical to those used in the previous study (Ferfouri et al. 2025) to ensure consistency in flow resolution.

Characteristic	Value
Total number of cells	3,055,200
Radial cell count	95
Circumferential cell count	80
Model cell count	412
Upstream domain length (cal.)	32
Downstream domain length (cal.)	53
Radial domain extent (cal.)	44

Table 1. 3D Computational domain characteristics.

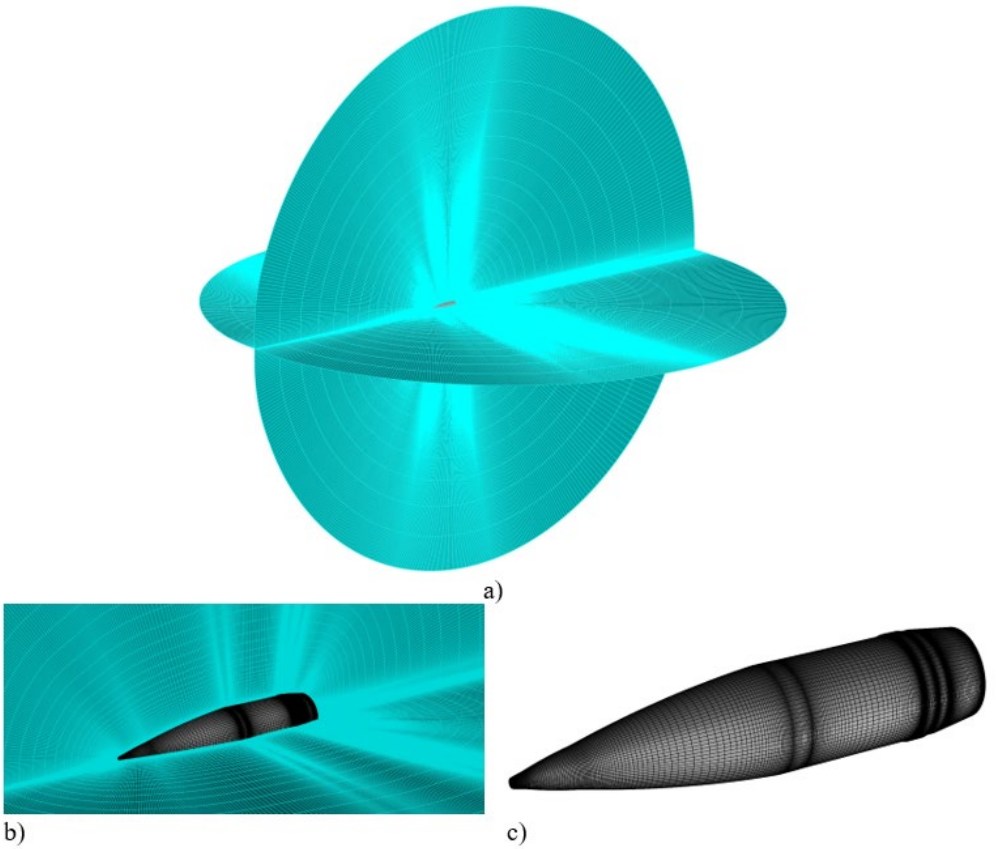

Fig. 2. 3D numerical domain: a) entire domain, b) near-field region around the projectile, c) surface grid of the projectile.

2.5 Numerical solver and convergence criteria

Numerical simulations are conducted using commercial CFD software, which uses the finite volume approach (FVM) to solve the RANS governing equations. For these steady-state 3D simulations, a density-based implicit solver is used in double-precision mode. This particular numerical method is preferred for high-speed compressible flows because it maintains stability without the intricate time-stepping procedures required by solvers based on pressure coupling (Nicolás-Pérez et al. 2017). The numerical process calculates the density distribution via the continuity equation and determines the pressure distribution using an appropriate equation of state. At the same time, the velocity components are computed by solving the momentum equations, which account for the various forces acting on the fluid. A zero-Pascal operating pressure is maintained throughout the computational domain. To accurately represent the near-wall flow characteristics of the projectile surface, the Enhanced Wall Treatment option is activated for the Realizable k-ε turbulence model, whereas this is handled automatically in the ω-equation-based model. The characteristic cross-sectional area and diameter are set to $S = 0.01887$ m² and $d = 0.155$ m, respectively.

An implicit formulation is used for the linearization of the governing equations, while the gradient terms are calculated with the Green–Gauss node-based method. A second-order upwind scheme is applied for spatial discretization. The Roe-FDS scheme (Roe 1986) is selected for the discretization of convective flux terms due to its proven effectiveness in resolving flows with significant compressibility effects (Nicolás-Pérez et al. 2017). To control the stability of the calculation, the CFL number (Courant et al. 1967) is adjusted between 1 and 200, depending on the complexity and nonlinearity of the flow at different Mach numbers. Solution stability is confirmed by monitoring both the residuals and the static aerodynamic coefficients. Convergence is officially reached once the residual values of all flow variables have dropped by at least 10^{-4}. Furthermore, C_X, C_N, and C_m must stabilize, showing a difference of less than 0.05% over the final 100 iterations. The 3D steady-state simulations were conducted using an 11$^{\text{th}}$-generation Intel i7-11800H processor running at 2.3 GHz with 8 cores. The typical computational time per iteration was approximately 9 seconds. The number of iterations required to reach these criteria typically ranges up to 2500, depending on the M_a number and the chosen turbulence model, resulting in a total time of roughly 6.3 hours for each simulation case.

3. Approach for determining aerodynamic coefficient derivatives

Before presenting the simulation results, it is first necessary to explain how the aerodynamic coefficient derivatives are determined. CFD simulations of the flow around the projectile enable the computation of aerodynamic force components (X, Y, N) and corresponding moments (l, m, n), as well as their corresponding coefficients (C_X, C_Y, C_N, C_l, C_m, C_n), expressed in the wind (aerodynamic) coordinate system. Subsequently, the static and dynamic aerodynamic coefficient derivatives are determined in accordance with Eqs. (5) and (6) (McCoy 1998; Regodić 2006; Carlucci & Jacobson 2018), taking into account the characteristic dependence of the aerodynamic coefficients on the non-dimensional spin rate p^* and on the quantity δ, defined as $\delta = \sin(\alpha)$, where α denotes the projectile's angle of attack:

$$R = \begin{bmatrix} X \\ Y \\ N \end{bmatrix} = q_\infty S_{ref} \begin{bmatrix} C_X \\ C_Y \\ C_N \end{bmatrix} = \frac{1}{2}\rho_\infty V_\infty^2 S_{ref} \begin{bmatrix} C_{X0} + C_{X\delta^2}\delta^2 \\ C_{Yp\alpha} p^* \delta \\ C_{N\alpha}\delta \end{bmatrix} \tag{5}$$

$$M = \begin{bmatrix} l \\ m \\ n \end{bmatrix} = q_\infty S_{ref} d \begin{bmatrix} C_l \\ C_m \\ C_n \end{bmatrix} = \frac{1}{2} \rho_\infty V_\infty^2 S_{ref} d \begin{bmatrix} C_{lp} p^* \\ C_{m\alpha} \delta \\ C_{np\alpha} p^* \delta \end{bmatrix} \tag{6}$$

The aerodynamic coefficients must be expressed in terms of the angle-of-attack α and the projectile spin rate p throughout the entire considered M_a range. Accordingly, the axial force coefficient C_X is expressed as a function of δ, whereas the spin-damping moment coefficient C_l is represented as a function of the non-dimensional spin rate p^*. C_X is modeled as a second-order even function, in which the coefficient of the quadratic term defines the derivative $C_{X\delta^2}$, as given by Eq. (5). Higher-order terms ($> \delta^2$) are omitted, as only small angles of attack are considered. C_l is proportional to the non-dimensional quantity p^* and is therefore represented by a linear function, such that the derivative C_{lp} corresponds to the slope of the associated curve.

Experimental wind-tunnel investigations conducted on a 140-mm caliber projectile across a M_a range from 0.5 to 2.5 have shown that the normal force coefficient C_N and its corresponding pitching moment coefficient C_m behave as predominantly linear functions of the AoA for values up to approximately 6° (Jenke & Shadow 1975). The same studies also indicated that the coefficient C_Y of the Magnus force and the coefficient C_n of the Magnus moment generally exhibit nonlinear behavior for angles of attack exceeding 4° and for non-dimensional spin rate greater than 0.15 (Jenke & Shadow 1975). Additional experimental investigations performed on a 155-mm caliber projectile, over an AoA range from 0° to 40°, demonstrated that C_N and C_m vary almost linearly with the angle of attack up to approximately 30° (Fresconi & Celmins 2018). When aerodynamic coefficients exhibit a linear dependence, their corresponding derivatives may be considered constant for a given Mach number. In such cases, these coefficients are represented as first-order odd functions, with the derivatives corresponding to the slopes of their respective curves.

However, when nonlinear behavior is identified, the derivatives must be evaluated not only as functions of the Mach number, but also in terms of the AoA and/or the non-dimensional spin rate p^*. In such cases, the aerodynamic coefficients (C_Y, C_N, C_m, C_n) are represented as third-order odd functions, as expressed in Eq. (7), where C_{Yp} and C_{np} represent the Magnus force and moment coefficient derivatives due to spin rate. Terms higher than the cubic order ($> \delta^3$) are neglected, consistent with the small angle-of-attack values considered. The corresponding derivatives for this formulation are defined by Eq. (8).

$$\begin{aligned} C_N &= C_{N\alpha_0} \delta + C_{N\alpha_2} \delta^3 \\ C_m &= C_{m\alpha_0} \delta + C_{m\alpha_2} \delta^3 \\ C_{Yp} &= C_{Yp\alpha_0} \delta + C_{Yp\alpha_2} \delta^3 \\ C_{np} &= C_{np\alpha_0} \delta + C_{np\alpha_2} \delta^3 \end{aligned} \tag{7}$$

The coefficients of the first-order terms in Eq. (7) represent the linear aerodynamic derivatives, whereas the third-order coefficients account for the cubic contributions. In accordance with the study objectives, only the formulations relevant to static aerodynamic derivatives ($C_{N\alpha}$, $C_{m\alpha}$) are employed.

$$
\begin{aligned}
C_N &= C_{N\alpha_0}\delta + C_{N\alpha_2}\delta^3 \\
C_m &= C_{m\alpha_0}\delta + C_{m\alpha_2}\delta^3 \\
C_{Yp} &= C_{Yp\alpha_0}\delta + C_{Yp\alpha_2}\delta^3 \\
C_{np} &= C_{np\alpha_0}\delta + C_{np\alpha_2}\delta^3
\end{aligned}
\tag{8}
$$

4. Results and discussion

Expanding on the validated numerical approach established in our previous 2D study (Ferfouri et al. 2025), this section evaluates the 3D asymmetric flow performance of the 155 mm M107 artillery projectile. While the previous study focused exclusively on zero-yaw axial force (drag) coefficient C_{X0}, the current work extends this analysis to determine the static aerodynamic coefficients (C_X, C_N, and C_m), which correspond to the axial force, normal force, and pitching moment, respectively. These numerical results, obtained using a steady-state RANS approach, are validated against experimental data obtained for the HE M107 projectile (McCoy 1998). Furthermore, since the M107 and M101 projectiles share identical geometric and inertial characteristics and differ only in the design of the rotating band (Karpov & Schmidt 1964), experimental results from M101 aeroballistic range tests (Karpov & Schmidt 1964) are also utilized for validation purposes. Following the conclusions of the 2D study (Ferfouri et al. 2025), the O-grid topology is applied in conjunction with both turbulence models, Realizable k-ε and the SST k-ω.

The investigation covers thirteen Mach numbers between M_a = 0.5 and M_a = 3.0, encompassing flight regimes ranging from subsonic through transonic to supersonic. Unlike the previous 2D axisymmetric case where the angle of attack was restricted to $\alpha = 0°$, this 3D steady-state analysis explores three distinct angles of attack, specifically 2°, 5°, and 8°. As a result, aerodynamic coefficients can be quantified with high accuracy over a broad spectrum of operating conditions.

4.1 Grid resolution independence analysis

The total number of cells reported in Table 1 was determined based on a grid independence analysis to establish a suitable mesh resolution for the computational domain. The results reported in the present analysis were generated using the Realizable k-ε turbulence model. The characteristics of the grids considered in this analysis are summarized in Table 2. The mesh refinement assessment was carried out for two M_a cases, M_a = 0.9 and M_a = 2.5. For M_a = 0.9, the analysis was performed at three angles of attack: 2°, 5°, and 8°. For M_a = 2.5, two angles of attack, 2° and 5°, were considered. For M_a = 0.9, the radial cell count was kept constant at N_{r1} = 95, while the cell count in the circumferential direction was adjusted in four steps, from $N_{\theta 1}$ = 40 to $N_{\theta 4}$ = 120. In the second stage, the circumferential grid resolution selected from the first phase was retained, and the cell count in the radial direction was modified in three steps, from N_{r1} = 95 to N_{r3} = 140. This procedure resulted in six distinct grid density levels. For M_a = 2.5, three grid density levels were examined, with the cell count in both the circumferential and radial directions increasing simultaneously for each level, as detailed in Table 2.

The results of the grid resolution analysis for M_a = 0.9 are presented in Tables 3 and 4, while those for M_a = 2.5 are reported in Table 5. The same methodology adopted for the 2D simulations (Ferfouri et al. 2025) was applied in this work. The percentage difference P_{dif} among the computed results was evaluated for each pair of consecutive grid densities over all considered angles of attack. A threshold P_{dif} value less than 2% was adopted as the criterion for achieving

grid-independent results. Table 3 presents the percent difference P_{dif} for $M_a = 0.9$ as the cell count in the circumferential direction increases. All computed P_{dif} values fall below 1% starting from the second circumferential grid density level. This indicates that the two finer grids, $G_{r1\theta3}$ and $G_{r1\theta4}$, which feature a higher circumferential resolution, provide only marginal improvement over grid $G_{r1\theta2}$ regarding the projectile aerodynamic characteristics. Consequently, a circumferential resolution of 80 cells, corresponding to grid $G_{r1\theta2}$, was selected for the subsequent analysis of grid refinement in the radial direction.

Grid	Total number of cells	Radial cell count (N_{ri})	Circumferential cell count ($N_{\theta j}$)
$M_a = 0.9$			
$G_{r1\theta1}$	1,546,600	95	40
$G_{r1\theta2}$	3,055,200		80
$G_{r1\theta3}$	3,942,120		104
$G_{r1\theta4}$	4,525,800		120
$G_{r2\theta2}$	3,698,400	115	80
$G_{r3\theta2}$	4,502,400	140	
$M_a = 2.5$			
$G_{r1\theta2}$	3,055,200	95	80
$G_{r2\theta3}$	4,772,040	115	104
$G_{r3\theta4}$	6,669,600	140	120

Table 2. 3D Domain Characteristics for Mesh Density Study.

Consecutive grid densities	α [°]	C_X [%]	$C_{N\alpha}$ [%]	$C_{m\alpha}$ [%]
$G_{r1\theta2}/G_{r1\theta1}$	2	-0.49	-4.54	0.55
	5	-0.50	-4.45	0.46
	8	-0.40	-4.36	0.37
$G_{r1\theta3}/G_{r1\theta2}$	2	-0.28	-0.69	0.23
	5	-0.32	-0.51	0.15
	8	-0.32	-0.45	0.12
$G_{r1\theta4}/G_{r1\theta3}$	2	0.16	0.41	-0.16
	5	0.25	0.18	-0.07
	8	0.29	0.06	-0.02

Table 3. P_{dif} values at $M_a = 0.9$ with increasing circumferential cell count.

Table 4 presents the percent difference P_{dif} for $M_a = 0.9$ and $\alpha = 2°$ as the radial cell count increases. It can be clearly seen that all P_{dif} values remain below 2%. Therefore, a radial resolution of 95 cells is sufficient, and no further refinement in the radial direction is required.

Consecutive grid densities	C_X [%]	$C_{N\alpha}$ [%]	$C_{m\alpha}$ [%]
$G_{r2\theta2}/G_{r1\theta2}$	-0.25	-1.78	0.70
$G_{r3\theta2}/G_{r2\theta2}$	0.32	1.36	-0.55

Table 4. P_{dif} values at $M_a = 0.9$ and $\alpha = 2°$ with increasing radial cell count.

Table 5 summarizes the percent difference P_{dif} obtained at $M_a = 2.5$ for successive refinements in both the radial and circumferential directions. The results correspond to the angles of attack of 2° and 5°. All computed P_{dif} values are below 2%, indicating that even at the

supersonic Mach number of 2.5, the use of 95 cells along the radial direction and 80 cells along the circumferential direction yields grid-independent results. Accordingly, and based on the results reported in the preceding tables, grid $G_{r1\theta2}$ was selected for the steady-state RANS simulations.

Consecutive grid densities	α [°]	C_X [%]	$C_{N\alpha}$ [%]	$C_{m\alpha}$ [%]
$G_{r2\theta3}/G_{r1\theta2}$	2	0.83	0.02	1.16
	5	0.76	0.07	0.23
$G_{r3\theta4}/G_{r2\theta3}$	2	0.72	0.12	0.07
	5	-0.67	-0.07	0.35

Table 5. P_{dif} values at $M_a = 2.5$ with increasing both radial and circumferential cell count.

4.2 Analysis of static aerodynamic coefficients

Following the choice of a suitable mesh density for the 3D calculations, the results for the M107 projectile are compared with experimental data from the literature (Karpov & Schmidt 1964; McCoy 1998) to verify the accuracy of the numerical model. This process begins by applying the extraction methodology presented in Section 3 to determine the static aerodynamic derivatives from the steady-state 3D simulations. A key goal of the present analysis is to assess the capability of the steady-state RANS approach in estimating projectile aerodynamic performance. To this end, the results of the two selected RANS models are assessed through a direct comparison with the experimental reference measurements over the entire M_a range.

4.2.1 Static aerodynamic derivatives extraction

To verify the consistency of the numerical data, static aerodynamic derivatives are determined by applying the curve-fitting procedure to the aerodynamic coefficients derived from steady-state RANS analyses. This process is essential for extracting reliable derivatives from the numerical results. The results presented here pertain to the Realizable k-ε model. The same procedure used to compute aerodynamic derivatives from the Realizable k-ε results was also applied to the steady-state outcomes obtained with the SST k-ω model. To demonstrate the reliability of this extraction, the regression results for the transonic regime ($0.8 \leq M_a \leq 1.2$) are illustrated in Figs. 3, 5, and 6. This specific Mach range is selected as a representative case because the transonic regime is characterized by highly non-linear flow behavior and significant changes in pressure distribution due to shock wave development.

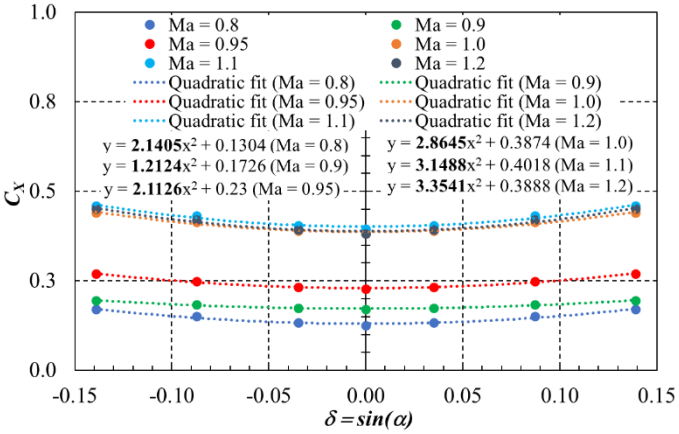

Fig. 3. C_X versus sin(α).

Figure 3 illustrates the C_X variation versus sin(α) in the transonic regime. To enhance the dataset, values corresponding to negative angles were included based on the symmetry condition $C_X(-\delta) = C_X(\delta)$ (Regodić 2006). The results clearly demonstrate that the evolution of C_X can be accurately modeled using a quadratic fit of the form $y = ax^2 + b$, with a coefficient of determination R^2 exceeding 0.97 for all investigated Mach numbers. In this expression, the constant a determines the value of the second-order derivative $C_{X\delta^2}$ (highlighted in bold in Fig. 3), while the constant b represents the axial force coefficient at zero-yaw, C_{X0}.

The C_{X0} results obtained from the previous 2D simulations (Ferfouri et al. 2025) were compared with those extracted from the 3D simulations through a quadratic fit of C_X versus δ, as shown in Table 6. These results correspond to simulations carried out with the Realizable k-ε model. It is found that the values derived from the fit are higher than those predicted by 2D simulations across all analyzed Mach numbers. This discrepancy is particularly evident within the transonic regime, where the percentage difference reaches approximately 7%. However, this finding requires further validation through additional 3D simulations performed specifically at zero-yaw.

Mach number	C_{X0} values		P_{dif}[%]
	2D (simulation)	3D (quadratic regression)	
0.50	0.131	0.141	7.09
0.60	0.128	0.137	6.70
0.70	0.128	0.134	5.25
0.80	0.123	0.130	6.02
0.90	0.168	0.173	2.56
0.95	0.226	0.230	1.75
1.00	0.380	0.387	1.82
1.10	0.393	0.402	2.18
1.20	0.379	0.389	2.55
1.50	0.336	0.347	3.22
2.00	0.284	0.294	3.31
2.50	0.245	0.254	3.52
3.00	0.218	0.226	3.29

Table 6. C_{x0} results from 2D simulations and 3D-derived regression.

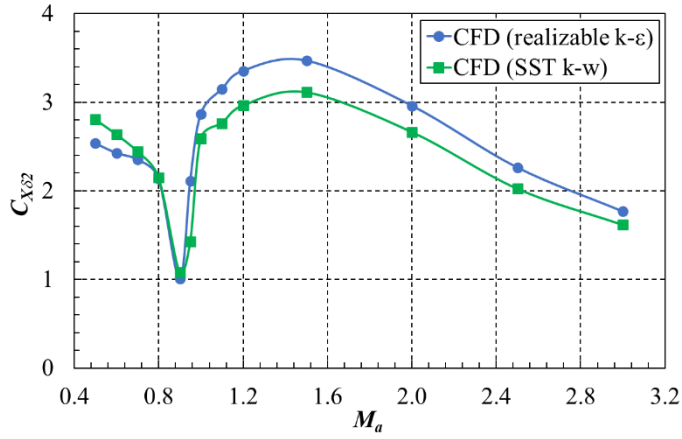

Fig. 4. $C_{X\delta^2}$ versus Mach number.

The quadratic fit of the numerical data also allows for the extraction of $C_{X\delta^2}$, as shown in Fig. 4. The results obtained using the two RANS turbulence models show distinct differences. Specifically, the Realizable k-ε model yields significantly higher values than the SST k-ω model, except within the M_a range from 0.7 to 0.9, where the results are nearly identical.

The variations in the normal force coefficient C_N and the pitching moment coefficient C_m with respect to the sine of the angle-of-attack are illustrated in Figs. 5 and 6 for the transonic regime. The results indicate that the evolution of both C_N and C_m follows a linear fit ($y = ax + b$) with an intercept nearly equal to zero ($b \approx 0$). This is consistent with the physical requirement that both coefficients C_N and C_m must be zero at zero-yaw due to the axisymmetric flow over the projectile. The slope of the fit determines the values of the aerodynamic derivatives $C_{N\alpha}$ and $C_{m\alpha}$ (highlighted in bold in Figs. 5 and 6), with a coefficient of determination R^2 of approximately 1 across all Mach numbers. This linearity demonstrates that both derivatives remain constant within the considered range of angle-of-attack. Consequently, for a potential trajectory analysis, these derivatives would be incorporated into the flight model exclusively expressed in terms of the Mach number.

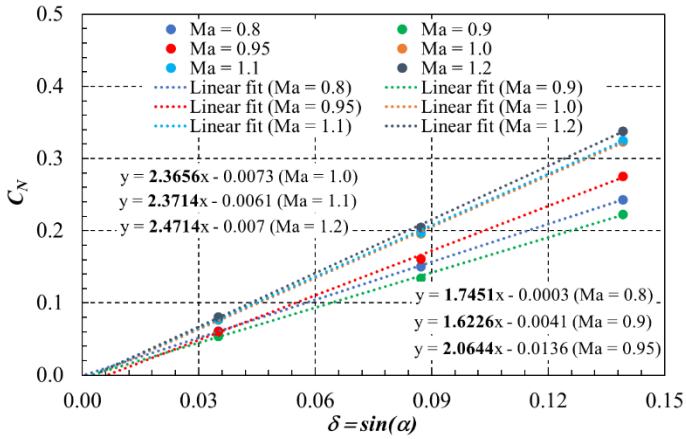

Fig. 5. C_N versus sin(α).

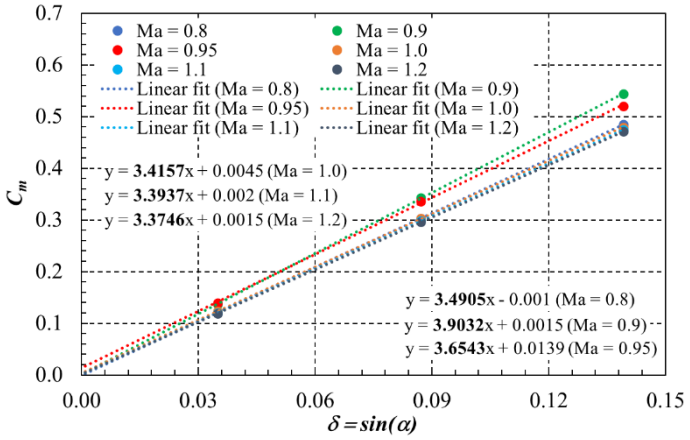

Fig. 6. C_m versus sin(α).

The close agreement between the CFD results and the theoretical formulations of the aerodynamic coefficients, specifically the quadratic even order behavior for C_X and the linear odd order trends for C_N and C_m, validates the robustness of the steady-state numerical approach. This high correlation demonstrates that the CFD methodology accurately captures the theoretical functional forms of the static coefficients under investigation. For the sake of conciseness, the fit plots in the subsonic and supersonic regimes are omitted, as they follow the same functional trends with high R^2 values, ensuring further confidence in the results obtained across the entire flight range.

4.2.2 Comparison with reference data

The numerical predictions obtained for static aerodynamic derivatives are evaluated against experimental reference measurements for both the M107 and M101 projectiles (Karpov & Schmidt 1964; McCoy 1998). This comparison aims to assess the performance of the RANS turbulence models, the Realizable k-ε and SST k-ω, under steady-state conditions, covering all projectile flow regimes from subsonic through supersonic. As previously noted, the M107 projectile differs from the M101 model only by its rotating band, meaning they share the same geometric and inertial characteristics (Karpov & Schmidt 1964). Consequently, besides the available experimental data for the M107, data for the M101 projectile are also employed to validate the numerical model. The experimental measurements for both projectiles were obtained from tests conducted in an aeroballistic range. The maximum expected percent errors for these results are presented in Table 7 and are included as error bars in the comparison of the results (DeSpirito & Heavey 2004; Silton 2005). For the experimental data at zero-yaw, specifically C_{X0}, the Mach number for the M107 projectile varies between 0.5 and 3.0, while for the M101 projectile, it varies between 0.5 and 2.5. Regarding the aerodynamic derivatives $C_{N\alpha}$ and $C_{m\alpha}$, the results for the M107 projectile correspond to a $M_a \approx 0.8$ and an AoA of 2.5°. For the M101 projectile, the $C_{N\alpha}$ and $C_{m\alpha}$ data cover a M_a range from 0.5 to 2.4, with AoA values of 2±0.5° and 3±0.5°.

Aerodynamic Coefficient	Percent error [%]
Axial force (C_X)	2
Normal Force (C_N)	10
Pitching Moment (C_m)	3

Table 7. Maximum expected percent errors of the static aerodynamic coefficients.

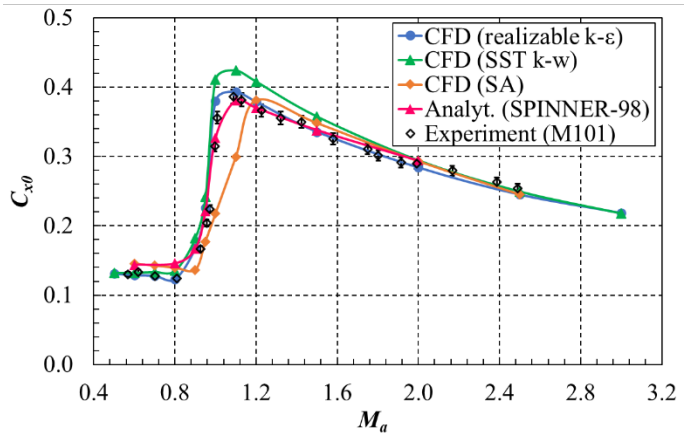

Fig. 7. C_{X0} versus Mach number.

Figures 7–9 illustrate a comprehensive comparison of the CFD results with experimental data for both the M101 and M107 projectiles across the specified M_a range. This analysis encompasses the axial force coefficient at zero-yaw C_{X0}, along with the normal force derivative $C_{N\alpha}$ and the pitching moment derivative $C_{m\alpha}$.

The comparative study of C_{X0} was specifically performed to verify the aerodynamic similarity between the M101 and M107 projectiles. This similarity is clearly corroborated in Fig. 7, where the experimental curves for both projectiles exhibit an almost perfect overlap. Furthermore, the previous 2D numerical simulations utilizing the Realizable *k-ε* turbulence model (Ferfouri et al. 2025) demonstrate an excellent correlation with the experimental measurements for the M101 projectile, validating the choice of the M101 projectile as a reference for the M107 validation.

As shown in Figs. 8 and 9, the 3D simulations conducted under steady-state conditions effectively predict the $C_{N\alpha}$ and $C_{m\alpha}$ derivatives throughout the considered Mach number range. Both RANS turbulence models yield results that remain almost entirely within the experimental error bars, offering robust confidence in the numerical predictions. In the supersonic regime, the predicted values for $C_{N\alpha}$ are slightly higher than the experimental data, while the $C_{m\alpha}$ values remain marginally lower across the entire range of Mach numbers. It can be seen that the outcomes of both RANS models are almost identical, with the exception of the transonic region between Mach 0.9 and 0.95, where slight discrepancies emerge due to the complex shock wave interactions characteristic of this regime.

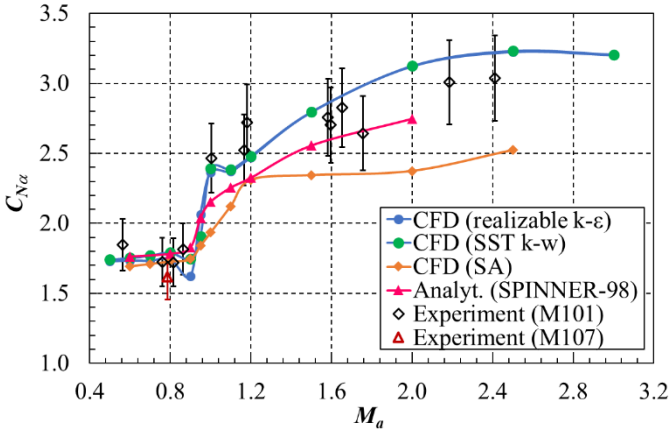

Fig. 8. $C_{N\alpha}$ versus Mach number.

A comparison with other studies is included to provide additional perspective on the present results, as shown in Figs. 7–9. Reference data are taken from an unsteady CFD investigation based on the Spalart–Allmaras (SA) turbulence model over a M_a range from 0.6 to 2.5 (Wessam & Chen 2015), as well as from a semi-empirical study relying on the SPINNER-98/PRODAS code over the M_a range from 0.6 to 2.0 (Khalil et al. 2009). For C_{x0}, the present steady-state 3D RANS predictions show improved agreement with experimental data in the transonic regime compared with the unsteady CFD investigation and remain consistent with the semi-empirical estimates. Regarding $C_{N\alpha}$, all approaches provide similar values in the subsonic regime. In the transonic regime, the unsteady CFD and semi-empirical predictions tend to lie well below the experimental measurements, while the present results remain close to the reference data. At supersonic Mach numbers, the unsteady CFD investigation does not reproduce $C_{N\alpha}$ values close to the reference data, the semi-empirical approach slightly underestimates $C_{N\alpha}$ but remains within the experimental uncertainty band, and the present simulations show a small overestimation. For $C_{m\alpha}$, predictions are comparable in the subsonic regime. The present results and the semi-empirical estimates remain in close agreement in transonic and supersonic conditions, whereas the unsteady CFD investigation tends to overpredict $C_{m\alpha}$, particularly at higher supersonic Mach numbers.

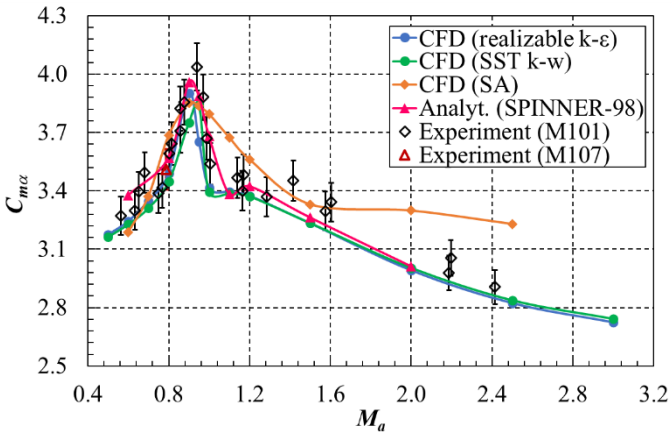

Fig. 9. $C_{m\alpha}$ versus Mach number.

The obtained numerical predictions show a superior level of agreement with the aeroballistic range measurements. The steady-state RANS models successfully capture the physical phenomena of the transonic drag rise and the subsequent stabilization in the supersonic regime. By utilizing the O-grid topology as recommended in the 2D preliminary study (Ferfouri et al., 2025), the 3D simulations provide a robust and reliable estimation of the projectile aerodynamic behavior under asymmetric flow conditions. These findings are in complete alignment with previous investigations documented in the literature (DeSpirito & Heavey 2004; Silton 2005; DeSpirito et al., 2009; DeSpirito 2017; Ko et al. 2020). Specifically, studies concerning smaller calibers (DeSpirito & Heavey 2004; Silton 2005; DeSpirito et al., 2009) have revealed that steady-state RANS models constitute a reliable approach for predicting static aerodynamic derivatives, as they sufficiently capture the mean flow characteristics required for such aerodynamic assessments. This validation confirms that the selected numerical settings are highly appropriate for predicting the static aerodynamic performance of 155 mm artillery projectiles.

5. Conclusion

This paper demonstrates that steady-state 3D RANS simulations can reliably predict static aerodynamic coefficients and derivatives for a 155 mm projectile across subsonic to supersonic conditions, covering a Mach range from 0.5 to 3.0. The validated O-grid mesh and the derivative-extraction procedure provide an accurate and reproducible CFD scheme for trajectory and stability assessments, enabling the reliable computation of static aerodynamic derivatives. Advancing from previous axisymmetric analyses to a full 3D steady-state RANS approach allowed the resolution of asymmetric flow fields and ensured accurate aerodynamic predictions across the examined Mach range.

The comparative analysis showed that both the Realizable k-ε and SST k-ω models provide good agreement with experimental measurements in subsonic, transonic and supersonic regimes. The study validated an optimized structured hexahedral mesh generated with Gambit based on the O-topology, ensuring grid-independent results for forces and moments at angles of attack of 2°, 5° and 8°. The numerical approach proved effective for extracting static derivatives that remain consistent with aeroballistic trends.

The proposed steady-state 3D RANS methodology, combined with the extraction procedure, constitutes an efficient tool for aerodynamic assessment of large-caliber projectiles. Future work can extend this approach to determine Magnus force and moment coefficients and their associated dynamic derivatives, confirming that the selected numerical settings are appropriate for producing high-fidelity data for trajectory prediction and flight stability analysis.

Despite the successful prediction of static aerodynamic coefficients, the study is limited to steady-state RANS simulations and does not account for dynamic effects such as transient flow phenomena, projectile spin interactions beyond low angles of attack, or advanced turbulence modeling approaches. Results are restricted to relatively small angles of attack and should not be extrapolated without caution from higher angles of attack or more extreme flight conditions.

Acknowledgements: This research has been supported by the University of Defence in Belgrade, Republic of Serbia within the Project No. VA/TT/1/24-26.

References:

Ansys Inc. (2013). *ANSYS Fluent Theory Guide*. Release 15.0, Canonsburg, PA.

Carlucci, D. E., & Jacobson, S. S. (2018). *Ballistics - Theory and design of guns and ammunition*. In CRC Press. CRC Press.

Chughtai, F. A., Masud, J., & Akhtar, S. (2019). Unsteady aerodynamics computation and investigation of magnus effect on computed trajectory of spinning projectile from subsonic to supersonic speeds. *The Aeronautical Journal*, 123(1264), 863–889.

Courant, R., Friedrichs, K., & Lewy, H. (1967). On the Partial Difference Equations of Mathematical Physics. *IBM Journal of Research and Development*, 11(2), 215–234.

DeSpirito, J. (2008). Effects of Base Shape on Spin-Stabilized Projectile Aerodynamics. *26th AIAA Applied Aerodynamics Conference*.

DeSpirito, J. (2017). CFD Aerodynamic Characterization of 155-mm Projectile at High Angles-of-Attack. *35th AIAA Applied Aerodynamics Conference*.

DeSpirito, J., & Heavey, K. (2004). CFD Computation of Magnus Moment and Roll-Damping Moment of a Spinning Projectile. *AIAA Atmospheric Flight Mechanics Conference and Exhibit*.

DeSpirito, J., Silton, S. I., & Weinacht, P. (2009). Navier-Stokes Predictions of Dynamic Stability Derivatives: Evaluation of Steady-State Methods. *Journal of Spacecraft and Rockets*, 46(6), 1142–1154.

Doraiswamy, S., & Candler, G. V. (2008). Detached Eddy Simulations and Reynolds-Averaged Navier- Stokes Calculations of a Spinning Projectile. *Journal of Spacecraft and Rockets*, 45(5), 935–945.

Ferfouri, A., Allouche, T., D. Jerković, D., Hristov, N., Vučković, M., & Benmeddah, A. (2023). Prediction of drag aerodynamic coefficient of the 155mm projectile under axisymmetric flow using different approaches. *Journal of the Serbian Society for Computational Mechanics*, 17(2), 69–86.

Ferfouri, A., Jerković, D. D., Hristov, N., Kari, A. V, & Allouche, T. (2025). Performance Analysis of Grid Topologies and RANS Turbulence Models in Predicting Aerodynamic Drag Coefficient at Zero-yaw for an Artillery Projectile. *Journal of Applied Fluid Mechanics*, 18(3), 585–600.

Fresconi, F., & Celmins, I. (2018). Experimental Flight Characterization of Spin-Stabilized Projectiles at High Angle of Attack. *AIAA Atmospheric Flight Mechanics Conference*.

ICAO. (1993). *Manual of the ICAO standard atmosphere extended to 80 kilometers (262 500 feet)*.

Jenke, L. M., & Shadow, T. 0. (1975). *Experimental magnus and static stability characteristics of ballistic projectiles with various boattail angles and lengths at Mach numbers from 0.5 through 2.5*.

Karpov, B. G., & Schmidt, L. E. (1964). The Aerodynamic Properties of the 155-mm Shell M101 from Free Flight Range Tests of Full Scale and 1/12 Scale Models. In *US Army Armament Research and Development Command, US Army Ballistic Research Laboratory*.

Khalil, M., Abdalla, H., & Kamal, O. (2009). Dispersion Analysis for Spinning Artillery Projectile. *13th International Conference on Aerospace Sciences and Aviation Technology*.

Ko, A., Chang, K., Sheen, D.-J., Lee, C.-H., Park, Y., & Park, S. W. (2020). Prediction and Analysis of the Aerodynamic Characteristics of a Spinning Projectile Based on Computational Fluid Dynamics. *International Journal of Aerospace Engineering*, 1–12.

McCoy, R. L. (1998). *Modern Exterior Ballistics*. Schiffer Publishing Ltd, ISBN: 978-0-7643-3825-0.

Menter, F. R. (1994). Two-equation eddy-viscosity turbulence models for engineering applications. *AIAA Journal*, 32(8), 1598–1605.

Nicolás-Pérez, F., Velasco, F. J. S., García-Cascales, J. R., Otón-Martínez, R. A., López-Belchí, A., Moratilla, D., Rey, F., & Laso, A. (2017). On the accuracy of RANS, DES and LES turbulence models for predicting drag reduction with Base Bleed technology. *Aerospace Science and Technology*, 67, 126–140.

Regodić, D. (2006). *Spoljna balistika*. Ministarstvo odbrane, Vojna akademija. Beograd.

Roe, P. L. (1986). Characteristic-Based Schemes for the Euler Equations. *Annual Review of Fluid Mechanics*, 18(1), 337–365.

Roy, A. (2012). *A First Course on Aerodynamics*. Ventus Publishing ApS.

Shih, T.-H., Liou, W. W., Shabbir, A., Yang, Z., & Zhu, J. (1995). A New k-ϵ Eddy Viscosity Model for High Reynolds Number Turbulent Flows. *Computers & Fluids*, 24(3), 227–238.

Silton, S. (2011). Navier-Stokes Predictions of Aerodynamic Coefficients and Dynamic Derivatives of a 0.50-cal Projectile. *29th AIAA Applied Aerodynamics Conference*.

Silton, S. I. (2005). Navier-Stokes Computations for a Spinning Projectile from Subsonic to Supersonic Speeds. *Journal of Spacecraft and Rockets*, 42(2), 223–231.

Wessam, M. E., & Chen, Z. H. (2015). Flow Field Investigations and Aerodynamic Characteristics of Artillery Projectile. *International Conference of Electrical, Automation and Mechanical Engineering.*